Experimental validation of optimization concepts for focal-plane image processing with adaptive optics

Visa Korkiakoski[a], Christoph U. Keller[a], Niek Doelman[b], Rufus Fraanje[c], Raluca Andrei[c] and Michel Verhaegen[c]

[a]Leiden Observatory, Niels Bohrweg 2, 2333CA Leiden, The Netherlands;
[b]TNO Science and Industry, Stieltjesweg 1, 2628CK Delft, The Netherlands;
[c]Delft Center for Systems and Control, Mekelweg 2, 2628CD Delft, The Netherlands

ABSTRACT

We show experimental results demonstrating the feasibility of an extremely fast sequential phase-diversity (SPD) algorithm for point sources. The algorithm can be implemented on a typical adaptive optics (AO) system to improve the wavefront reconstruction beyond the capabilities of a wavefront sensor by using the information from the imaging camera. The algorithm is based on a small-phase approximation enabling fast numerical implementation, and it finds the optimal wavefront correction by iteratively updating the deformable mirror. Our experiments were made at an AO-setup with a 37 actuator membrane mirror, and the results show that the algorithm finds an optimal image quality in 5–10 iterations, when the initial wavefront errors are typical non-common path aberrations having a magnitude of 1–1.5 rad rms. The results are in excellent agreement with corresponding numerical simulations.

Keywords: Adaptive optics, phase diversity, small-phase approximation

1. INTRODUCTION

When imaging objects through atmosphere, the turbulence distort the images. This is a common problem in astronomical observations as well as the limiting factor in current long distance surveillance cameras. To compensate this issue, both real-time techniques like adaptive optics[1] and post-facto image reconstruction techniques[2–4] have been extensively studied.

The problem of adaptive optics, in particular when trying to increase image resolution over large field of views, is that the optical systems easily become complex and expensive. On the other hand, the problem with the post-facto approaches, like phase-diversity,[2, 3, 5–8] is that it is computationally extremely demanding.

In our earlier work, we have shown that the combination of AO into traditional phase-diversity techniques offers a lot of potential in reducing the computational demands.[9] An alternative approach to design inexpensive ways to improve simple AO systems would be using the phase-diversity inspired focal-plane wavefront sensing techniques to drive the deformable mirror. Such ideas, called sequential phase diversity (SPD), have been proposed at a general level,[10, 11] but to our knowledge no detailed implementations have been published.

In this work, we will demonstrate that the sequential phase diversity is a viable concept. As a first step, we will concentrate on a technique working with point sources. It is described in detail in Section 2, and more physical insight are given in our another paper.[12] Section 3 describes the experimental arrangements we have done to validate the concept, and the results are shown in Section 4. Finally, the relevance of the experiments is discussed in Section 5.

Further author information: (Send correspondence to V.K.)
V.K.: E-mail: korkiakoski@strw.leidenuniv.nl

2. SEQUENTIAL PHASE-DIVERSITY ALGORITHM

This section describes in detail how we implement the sequential phase diversity (SPD). Our approach is based on a modified version of the small-phase solution to phase-retrieval problem proposed by.[13] Physical insight and more details of the approach can be found in.[12]

When assuming that the unknown wavefront error is small enough (less than a radian WF rms), it is possible to approximate the complex amplitudes in pupil plane as a linear function of the wavefront. This linear approximation, combined with a sequence of images with controllable WF differences, is sufficient to design a computationally efficient algorithm that can iteratively correct the WF aberrations, using only the focal plane images as a wavefront sensor.

Gonsalves proposed using a small-phase approximation

$$H = A(1 + iT), \tag{1}$$

where H is complex field at the pupil plane, i is imaginary unit, and T is the wavefront. While this expression is a useful starting point in designing algorithms based on small-phase approximations, it gives no practical details how to deal with the energy conservation — the normalized PSF energy should be constant and independent of the phase.

We will show that good results can be obtained by approximating the complex amplitudes as

$$H = \alpha^{1/2}A + iAT, \tag{2}$$

where α is the Strehl ratio of the intensity-normalized PSF. This approximation explicitly tells how to model the fact that the maximum of a distorted intensity image is lower than in the diffraction limited PSF.

The approximation leads to very similar equations as in,[13] enabling the phase retrieval by two successive Fourier transforms. We use the same notations as in,[13] and we denote the odd and even parts of the wavefront T as T_o and T_e. Respectively, the PSF ($|\mathscr{F}\{H\}|^2$) is broken to p_o and p_e. Thus, the phase can be solved by knowing that

$$y = \frac{p_o}{2\alpha^{1/2}a} \approx \frac{p_o}{2a} \tag{3}$$

and

$$v^2 = p_e - \alpha a^2 - y^2, \tag{4}$$

where y is the imaginary part of $\mathscr{F}\{AT_o\}$, and v is the real part of $\mathscr{F}\{AT_e\}$. We also apply regularization by substituting the division by a by a multiplication of $a/(a^2 + e)$, where e is a sufficiently small number.

We solve the sign ambiguity in Eq. (4) by using sequential phase diversity. We update the DM state at each iteration, and we aim to correct the WF aberrations as well as possible. Therefore, at each time step k, we know the current and previous image $(p(k), p(k-1))$ and the Fourier transforms of odd and even parts of the change in DM shape $(y_d(k), v_d(k))$. In addition, the odd WF components in Fourier space, $y(k)$ and $y(k-1)$, are trivial to obtain by using Eq. (3).

Then, we assume that the following relations hold for the even image components,

$$p_e(k - 1) = \alpha(k-1)a^2 + [y(k) + y_d(k)]^2 + [v(k) + v_d(k)]^2, \tag{5}$$

$$p_e(k) = \alpha(k)a^2 + y(k)^2 + v(k)^2. \tag{6}$$

It is seen that the p_e is dominated by a large term αa^2, and even slight errors in determining the correct value of α will have a big impact when computing the difference between $p_e(k-1)$ and $p_e(k)$. Therefore, we scale their values to an equal maximum value ($\max\{a^2\}$), and we assume the first terms in Eqs. (5) and (6) cancel each other in subtraction. This permits us to estimate the signs of v as

$$s(k) = \text{sign}\left\{\frac{v_d}{v_d(k)^2 + e}\left[\max\{a^2\}\left[\frac{p_e(k)}{\max\{p_e(k)\}} - \frac{p_e(k-1)}{\max\{p_e(k-1)\}}\right] - y_d(k)^2 - 2y(k)y_d(k) - v_d(k)^2\right]\right\}. \tag{7}$$

Then, the computation of even WF components at iteration k is done using Eq. (4),

$$v(k) = s(k) \left[\left| p_e(k) - \alpha a^2 - y(k)^2 \right| \right]^{1/2},$$ (8)

where the absolute values are introduced to avoid problems with small numeric errors.

At the first iteration, Eq. (7) cannot be used, so we use the signs of non-perturbed complex amplitudes in image plane ($s(1) = \text{sign}\{a\}$).

As soon as the $y(k)$ and $v(k)$ are obtained, we take Fourier transforms to obtain AT_o and AT_e. To avoid noise propagation, we apply here low-pass filtering using Gaussian windows with a size of 194×194. This is not necessarily an optimal size, but it gives sufficiently robust performance.

Then, we apply WF correction, using DM, to compensate exactly this amount of wavefront error. It appears that the WF estimates produced this way are somewhat underestimated, so it is not necessary to reduce the loop gains used in the feedback loop to avoid over-shoot and stability issues. The underestimation is not severe, and it gets compensated in closed-loop operation.

The major computational requirements in the WF reconstruction come from the Fourier transforms. Two FFTs are needed to obtain AT_o and AT_e, and, in addition, one FFT is needed to transform applied WF change from phase space to y_d and v_d. Besides of the FFTs, also additional algebraic operations are needed to transform the phase into DM actuator commands.

3. EXPERIMENTAL SETUP

This section describes the experiments we have conducted to validate the algorithm described in the previous section.

We use a standard, pre-aligned, adaptive optics kit from Okotech.[14] The setup contains a monochromatic light source, 37-actuator membrane mirror, Shack-Hartman wavefront sensor and an imaging camera. The details are shown in table 1.

We investigated the beam quality in the setup by looking at the amplitudes of the SH-WFS spots. It appears the beam has approximately a Gaussian shape, the center is shifted about $30 \times 30\%$ from the on-axis position, and the amplitudes at the edges are about 30–60% of the maximum intensity. However, we have made no attempts to take this into account in the simulations or SPD implementation.

At first, we use both the WFS and DM to calibrate the system to be able to accurately introduce arbitrary wavefront shapes with the mirror. We estimate actuator influence functions using the WFS, and then create mirror modes that are best fits to the Karhunen-Loeve modes[15] computed by yao.[16] To avoid noise propagation and excessive fitting errors, we restrict our controlled modes to the 20 lowest order mirror modes.

The details of these procedures can be found in numerous references, for instance.[1, 17, 18]

The SPD algorithm has then been then tested by only using the focal plane camera images to compute the iterative WF corrections.

Since the DM can correct only a very limited amount of WF stroke, we decided not to make any tip/tilt (TT) correction by the mirror. Instead, we change the clipping of the image array: at each iteration, we choose an array of 128×128 pixels having the center-of-gravity of measured PSF in the middle. This clipped array is then fed to the SPD computation.

In the SPD computations, we model the pupil and phase by arrays of 128×128 pixels. The pupil is assumed to be circular and having a perfect top-hat shape. To obtain the correct PSF pixel scale, we are using FFT arrays of 388×388 pixels.

Table 1. Parameters of experimental setup

DM	15 mm OKO Mirror
DM type	micro-machined membrane
number of actuators	37
controlled mirror modes	20
WFS	Shack-Hartmann
subaperture geometry	hexagonal
active sub-apertures	121
subaperture size	50 pix (diameter)
subaperture spot size	10 pix (FWHM)
Light source	monochromatic laser diode
wavelength	633 nm
imaging camera	Basler piA640-210gm
image resolution	640×480
Pixel Size	7.4 μm
Pixel Bit Depth	12 bits
Perfect PSF FWHM	3.0 pix

4. RESULTS

The algorithm performance, throughout this section, is measured by estimating the Strehl ratio as a function of iteration. Due to ease of implementation, the Strehl estimation is done by pure maximum comparison of intensity images normalized to same energy. Although the images are cut to a small size (32×32 pixels) containing the PSF core, it is known that this estimation is prone to errors of approximately 2–10%.[19] However, the given Strehl values work perfectly as indicative performance measure.

Throughout this section, we consider the performance in six selected noise cases to study the algorithm's robustness. We select three different exposure times, and for each exposure time we consider two cases: a single exposure and an average of 32 images. Each case results in different noise levels, but essentially all are limited by the CCD read-out noise and the dynamic range of the camera. Therefore, we will report the noise simply as the relative rms value of the maximum image intensity. Those values are enumerated in Table 2.

Table 2. Log relative noise rms values

exposure $\rightarrow$ max intensity	1 image	32 images
400 $\rightarrow$ 1300	-2.3	-2.9
750 $\rightarrow$ 2400	-2.6	-3.1
1100 $\rightarrow$ 3600	-2.7	-3.3

The values shown in Table 2 (averaged maximum image intensity and relative noise rms with respect to the maximum intensity) are estimated from the measurements at the AO kit. We have used those values to determine the noise statistics in our simulations. All the simulations shown in this section are made with both photon-shot noise following Poisson distribution, as well as with additive Gaussian read-out noise.

4.1 Comparison of SPD algorithms

At first, we compare the expected performances of two types of SPD implementations. We test two ways to normalize the PSF in the used approximations. The first case is done is discussed in Section 2. In second case, we assume the measured PSF is normalized to the same energy as diffraction limited PSF, but no Strehl normalization is done (the value of α in Eq. (2) is assumed to be unity).

We run simulations with parameters identical to the system discussed in Section 3 (static system, SPD is used to calibrate non-common path aberrations). We assume that the initial WF rms error is 1.2 rad, and it is corrected iteratively by SPD. We test two cases: relative noise rms (ratio of the maximum intensity) is $10^{-2.7}$ and $10^{-3.4}$. For each case, we do 8 identical simulation realizations. The results are shown in Fig. 1.
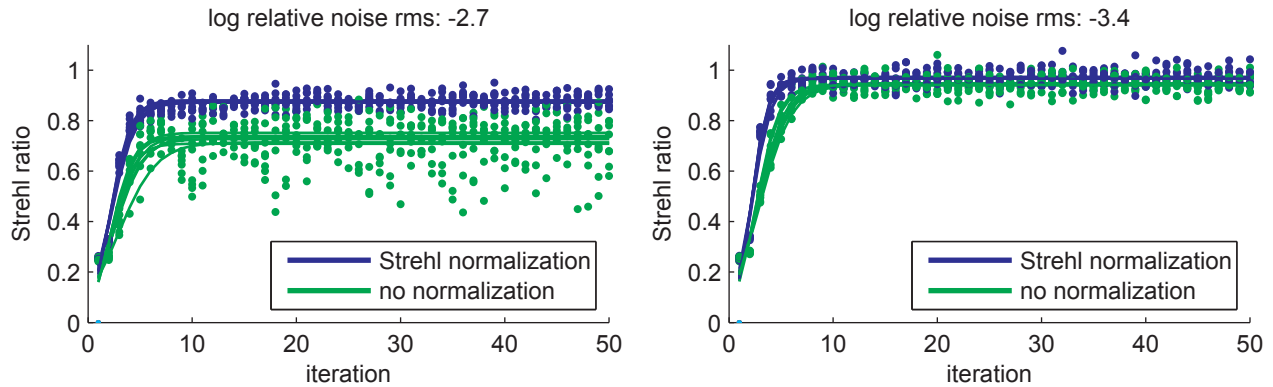
Figure 1. Comparison of SPD algorithms with and without Strehl normalization: Strehl ratio as a function of iteration. Dots show the simulated data points, lines are fits of sigmoid functions. 8 simulation runs are done for each set of parameters.

It is seen that normalizing the Strehl in SPD computations improves the performance. In the high-noise case, the mean of final converged Strehl increases from ~0.74 to ~0.88, and also robustness improves: the converged Strehl ratios vary within [0.80, 0.94] instead of [0.50, 0.90]. In addition, the algorithm converges almost 2 times faster. In the high-noise case the mean improves 2.5% and speed in convergence is still at least 30%.

4.2 Limiting factors in SPD performance

Next, we show the SPD results recorded by the optical setup.

At first, the deformable mirror is set to an initial condition by setting the actuator voltages to approximately at the middle of their operating range, and we align the optical components to optimize the image quality at the imaging camera. The wavefront sensor is calibrated to have this as a reference position. At our setup, this results in non-common path aberration errors that we estimate to be approximately 1.2 rad rms. Then, SPD is used to calibrate these errors.

We tried to reach the best performance that the SPD can reach at our AO setup, so we have used the low-noise case: highest possible exposure time, and each image fed to SPD is an average of 32 single-exposure images. Fig. 2 shows the five first images we recorded, and it is seen that five iterations are sufficient to dramatically improve the Strehl ratio: it increases from 0.30 to 0.80.
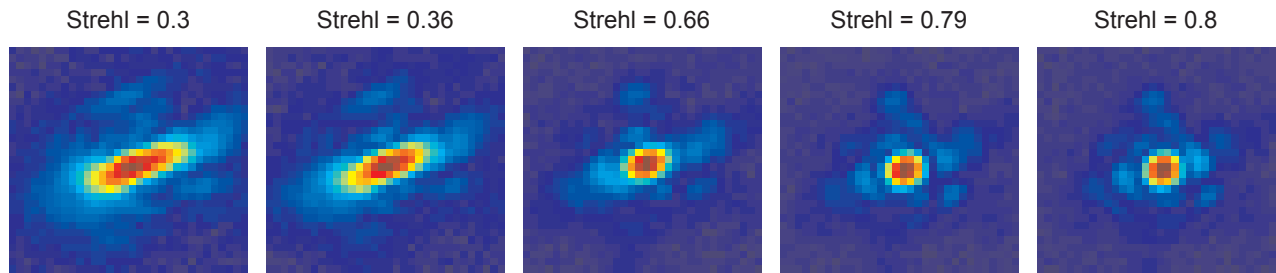
Figure 2. An example of the convergence with the sequential phase-diversity imaging. Relative noise rms is $10^{-7.5}$. 1st image shows the non-common path aberrations, and the last shows the image after 5 iterations.

We also wanted to compare the measured final image to simulations. We assumed that the WF rms error at uncorrectable high spatial frequencies is 0.36 rad (randomly distributed on 96 Zernike modes), and run the

SPD algorithm on simulated images having the same noise level. Fig. 3 shows the resulting images, that can be obtained after about 6–9 iterations.
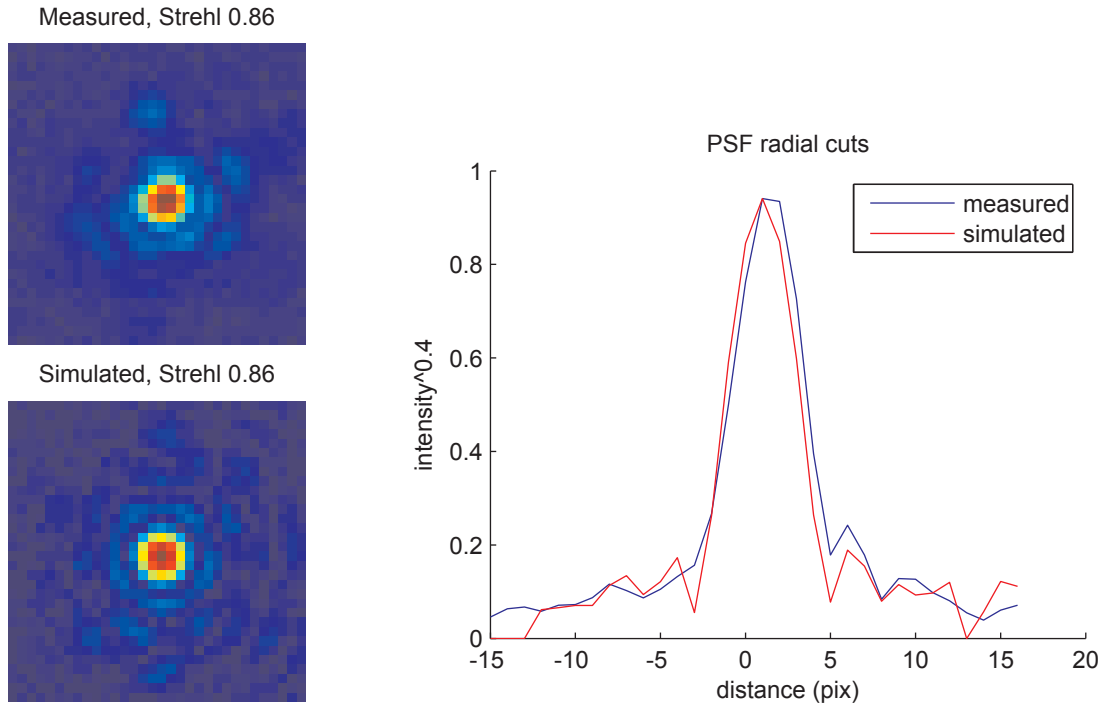
Figure 3. Examples of final image quality. Relative noise rms is $10^{-7.5}$. Upper right: measured intensity image (nonlinear scale). Upper left: simulated image. Lower: comparison of radial profiles.

Visual inspection shows that first diffraction ring is fully visible (although a bit clumpy), and the fragments of the second ring can be seen, in particular in the measured image. Both simulation and measured image have the same Strehl ratio of 0.86, but clearly different features can be seen to cause the errors.

In the simulated image, almost all of the remaining errors are at the high spatial frequencies that are not corrected by mirror modes. In the measured image, an unknown amount of errors is left in the correctable space. This could explain that the rings seem more smooth in the measurement. Besides, we believe the brighter blobs around the second ring of the recorded image could be ghost reflections from the beam splitter and/or reflected light from other parts of the optics.

To further investigate the limitations at our AO setup, we studied the final image quality as a function of the noise level. We compared the Strehl estimates of the recorded images to similarly computed estimates from simulations where the uncorrectable component of high spatial frequencies have 0.34, 0.36 and 0.40 rad rms WF error. The results are shown in Fig. 4.

It is seen that the measured Strehl can be increased by reducing the relative noise rms until about $10^{-2.6}$, and lower noise levels are not improving the results. The simulations predict that an increase of 3% should still be possible, and we conclude that the limiting factors are systematic errors that can be difficult to reduce: estimation errors caused by light reflected from other components and modeling errors (e.g, sensor pixels scale and diffraction limited PSF).

In addition, we see that the Strehl ratios estimated from the measurements vary much more than the simulated ones: their standard deviation is ~10 times higher. This issue is discussed in more detail in the following section.

Since we cannot accurately determine the estimation error at the controllable lower spatial frequencies, it is neither possible to estimate the error at higher spatial frequencies. Based on the simulations show in Fig. 4, we believe it to be between 0.34 and 0.40 rad rms. In the following, the value of 0.36 rad is used.
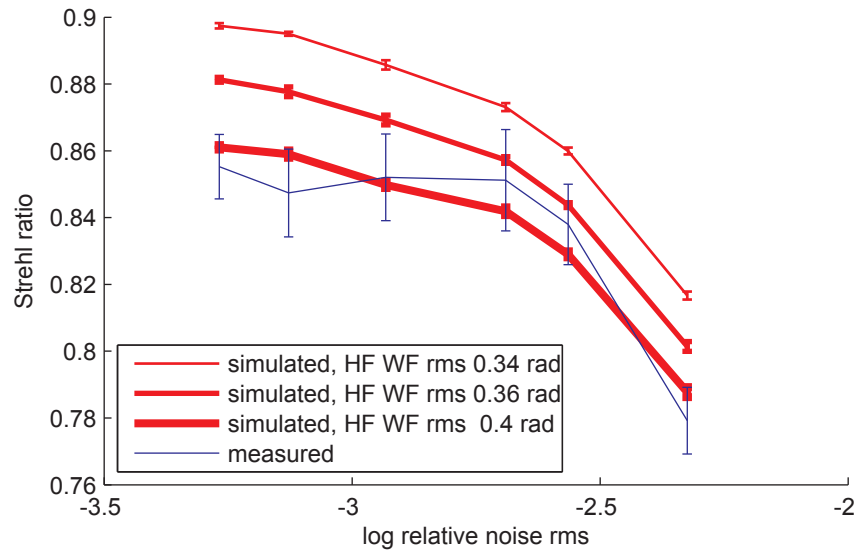
Figure 4. Final Strehl ratio as a function of relative noise rms. The noise rms is shown as ratio of the maximum image intensity.

4.3 SPD convergence properties

Next, we study in more detail the convergence properties of the SPD algorithm. We consider three cases, where the initial correctable WF error is 1.2, 1.5 and 1.9 rad rms. In the first case, all the errors are caused by the non-common path aberrations, and the two latter cases have additional aberrations introduced by the deformable mirror.

Fig. 5 shows the estimated Strehl ratios of the first 100 iterations in the selected cases.

It can be seen that the estimated Strehl ratios from both measured and simulated data sets agree very well. The SPD algorithm converges to the Strehl ratio of 0.85. The convergence takes about 5 iterations at initial aberrations of 1.2 rad and about two times longer with initial aberrations of 1.5 rad. When the initial aberrations are made larger, the algorithm starts to fail since the used approximation in Eq. (2) is no longer valid.

Fig. 5 also shows the same effect seen earlier in Fig. 4: the variance of the mean converged Strehl ratios is much larger in the measured data compared to the simulations. It is seen that the noise-induced Strehl variations within each individual SPD runs are almost identical, and therefore the errors in noise modeling do not explain the difference in the converged Strehl ratios.

Instead, most of the larger variations can be explained by errors in tip/tilt correction. As we do not correct tip/tilt by the deformable mirror (but instead change the clipping region), we do introduce an effect that the SPD WF reconstruction sees as a TT error. The recorded data shows that the location of the clipping array gets fixed after a few iterations, and it will not change at the later iterations. However, the clipping location has a ± 2 pixel variation between the different SPD runs. This explains the variation in converged Strehl values. The residual TT will distort the SPD WF reconstruction and introduces a decrease in the estimated Strehl ratio. The reasons for the different convergence patterns need to be investigated further, but we believe that improved TT correction would fully eliminate the clipping issue.

As also seen in Fig. 5, the algorithm stability is compromised when the initial WF aberrations are increased to 1.9 rad rms. Fig. 5 shows only the case at one noise level, and the fail rates at all noise levels, based on 8 SPD run on identical parameters, are enumerated in Table 3.

The table shows that the simulations fail 2–4 times more often than the experiments on our AO setup, which could be explained by the inaccuracies in determining the actual initial WF aberrations. In addition, it is seen that the measured SPD runs are 2–3 times more likely to fail at the low-noise compared to the medium-noise cases. This could be explained by the control issues in the feed-back loop. We are using a constant loop-gain
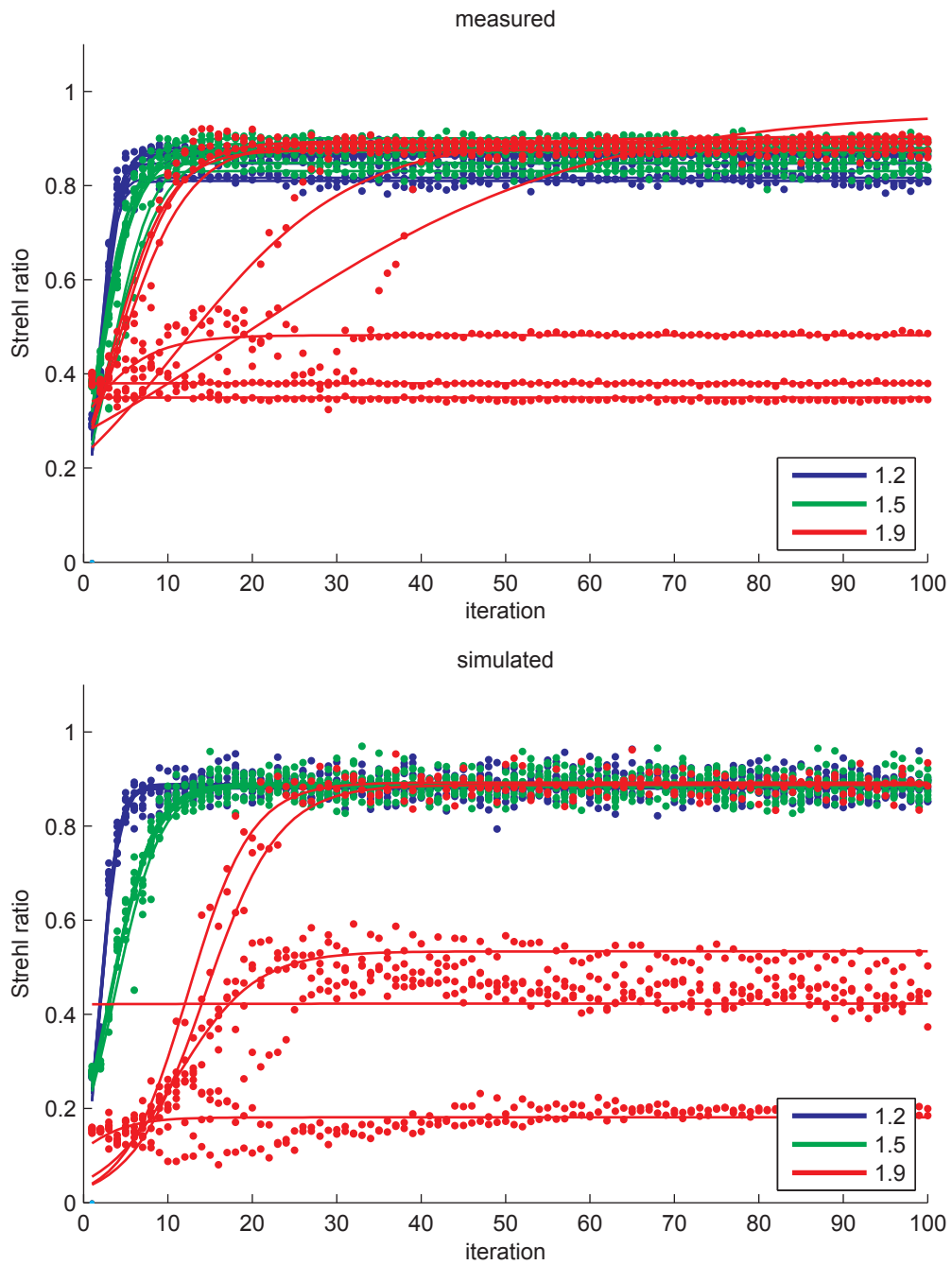
Figure 5. Illustration of algorithm convergence properties: Strehl ratio as a function of iteration. Relative noise rms is $10^{-2.9}$. Colors show the initial wavefront rms error (1.2, 1.5, 1.9 or 2.1 rad). Points show individual estimations and lines are fits to a sigmoid function. Eight different realization runs are done. Upper plot: measured data. Lower plot: simulated data.

Table 3. SPD fail rates with initial aberration of 1.9 rad rms

noise	-3.3	-3.1	-2.9	-2.7	-2.6	-2.3
measured	0.62	0.38	0.38	0.25	0.12	1
simulated	0.88	1	0.75	0.88	0.88	0.75

of one, and we are not optimizing our phase reconstruction by taking into account that the noise will effectively decrease the magnitude of the reconstruction leading to underestimation. A sensitivity correction, similar to the one proposed in,[20] could perhaps be used to further improve the performance.

A similar drop in performance is seen when we study the number of required iterations that is needed to reach the convergence. We define the convergence to be the point where a sigmoid function fit to estimated Strehl ratios reaches 95% of the maximum value of the fit. These convergence iterations are shown in Fig. 6 as a function of noise level.
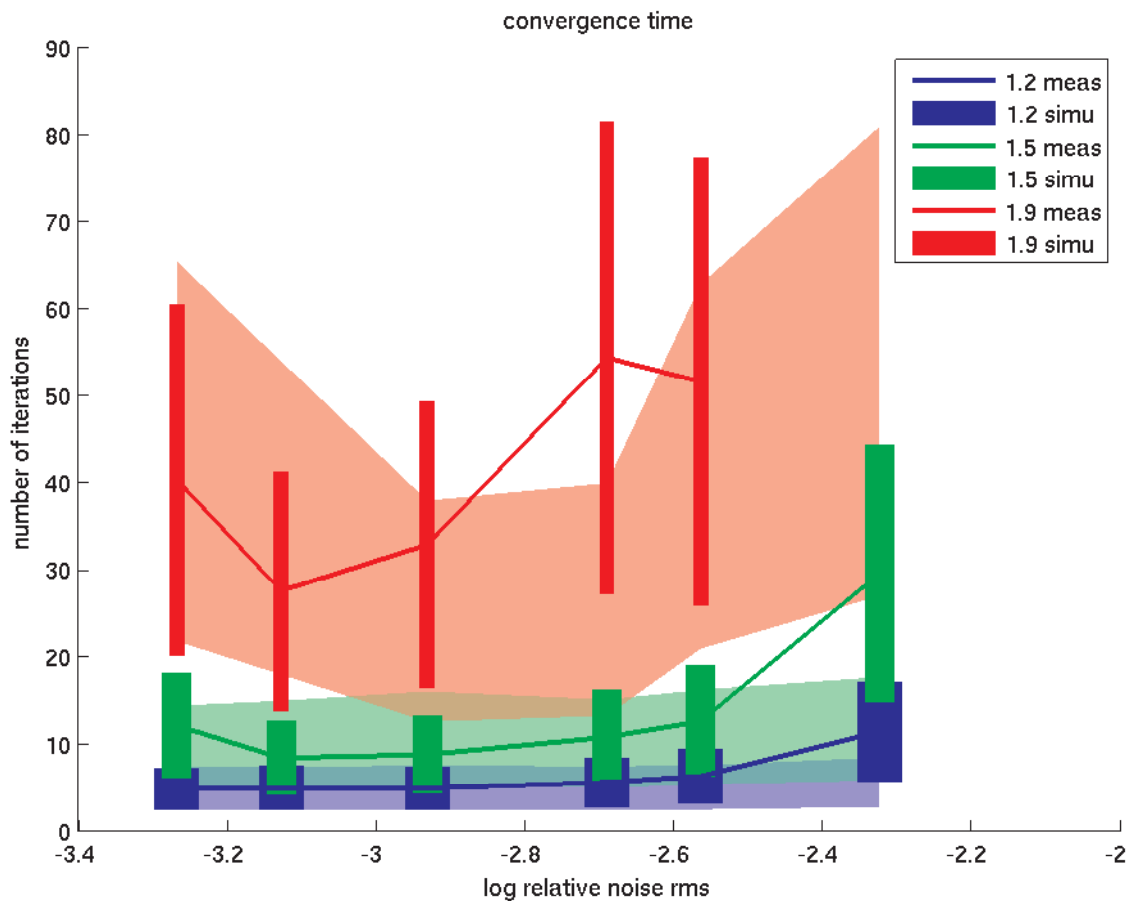
Figure 6. Number of required convergence iterations as a function of noise level. Colors show the initial wavefront rms error (1.2, 1.5, 1.9 or 2.1 rad). Line plots are from measured data, filled areas show the simulation results.

Both measurements and simulations show that as long as the relative noise level is lower than $10^{-2.9}$–$10^{-2.7}$, the SPD algorithm performs optimally when the initial WF aberrations are 1.2 or 1.5 rad rms. 4–6 iterations are needed in the former case and 8–18 iterations in the latter case. If the amount of noise is increased to $10^{-2.1}$, it can be necessary to iterate 2–3 times longer. If the amount of the initial aberrations is 1.9 rad rms, it is necessary to make 18–60 iterations, depending on the noise level, to reach the final Strehl ratio.

In addition, it is seen — similarly to Table 3 — that the performance is optimal at medium instead of lowest noise levels. Again, we believe this can be explained by the non-optimal control tuning of the feedback loop.

5. CONCLUSIONS

We have described in detail a sequential phase-diversity algorithm, and we studied its properties in simulations and actual experiments. The described SPD algorithm is computationally efficient — only three FFTs (and a few additional pixel-wise algebraic operations) are required to transfer the measured intensity images to the wavefront.

The algorithm converges from 1.2 rad WF rms error to the optical performance limit in about 4–6 iterations, which is comparable to the performance that a sensitive and non-linear pyramid wavefront sensor would give in similar conditions.[20] If we assume that an existing AO system can deliver a residual wavefront with 1.5 rad rms error, we could easily boost its performance by implementing the SPD algorithm to further correct the turbulence in real-time. This would be possible by using the current off-the-shelf hardware.

To our knowledge, this is the first time, when a complete and well-documented demonstration of fast focal-plane sensing algorithm has been published at this extent.

We have shown that the algorithm works well, and it is robust to correct typical non-common path aberrations at a simple low-order adaptive optics system. The algorithm corrects well 20 lowest mirror modes (being best least squares fits to Karhunen-Loeve modes) at noise levels where the rms of the additive read-out noise is less than 0.1% of the maximum intensity. This is easily achievable with current camera technology.

However, a few additional and challenging steps are still needed to bring the technology to the point where its performance at a wider range of applications is ultimately demonstrated. At least the following crucial points still needs to be addressed.

1. The algorithm works only at point sources. We plan to study options to apply deconvolution and iterative techniques to extend the technique also for extended sources.

2. The algorithm works only with monochromatic sources. It is necessary to study options how to deal with the PSF blurring that is caused by polychromatic light.

3. Optimization of the feedback loop has to be addressed. To get the best performance with SPD, it is necessary to put attention on the control issues. At least the following parameters have to be optimized: loop gains when applying the DM correction, regularization coefficient e (in the inversion to compute y), low-pass filtering window size (when computing AT_o and AT_e) and possibly also the approximation type (either $H = \alpha^{1/2}A + iAT$ or $H = \alpha^{1/2}A(1 + iT)$).

In addition, it is can also be necessary to pay attention to the issue of phase-to-actuator mapping. We need to find an efficient way to solve the relationship between wavefront shape and actuator commands to actually correct the distorting phase. This issue becomes more important when the number of actuators is increased and the actuators have strong cross-couplings.

Acknowledgments

REFERENCES

[1] Roddier, F., [*Adaptive Optics in Astronomy*], Cambridge university press, Cambridge (1999).
[2] Paxman, R. G., Schulz, T. J., and Fienup, J. R., "Joint estimation of object and aberrations by using phase diversity," *Journal of the Optical Society of America A* **9**, 1072–1085 (July 1992).
[3] Löfdahl, M. G. and Scharmer, G. B., "Wavefront sensing and image restoration from focused and defocused solar images," *Astronomy and Astrophysics Supplement* **107**, 243–264 (Oct. 1994).

[4] Paxman, R. G., Seldin, J. H., Löfdahl, M. G., Scharmer, G. B., and Keller, C. U., "Evaluation of Phase-Diversity Techniques for Solar-Image Restoration," *The Astrophysical Journal* **466**, 1087–+ (Aug. 1996).

[5] van Noort, M., Rouppe van der Voort, L., and Löfdahl, M. G., "Solar Image Restoration By Use Of Multiframe Blind De-convolution With Multiple Objects And Phase Diversity," *Solar Physics* **228**, 191–215 (May 2005).

[6] Sauvage, J., Fusco, T., Rousset, G., and Petit, C., "Calibration and precompensation of noncommon path aberrations for extreme adaptive optics," *Journal of the Optical Society of America A* **24**, 2334–2346 (Aug. 2007).

[7] Jefferies, S. M., Lloyd-Hart, M., Hege, E. K., and Georges, J., "Sensing wave-front amplitude and phase with phase diversity," *Applied Optics* **41**, 2095–2102 (Apr. 2002).

[8] van Eekeren, A. W., Schutte, K., Dijk, J., and Schwering, P. B., "Time-varying phase diversity turbulence compensation," in [*Infrared Technology and Applications XXXVII*], *Proc. SPIE* **8012**, 80120D (2011).

[9] Korkiakoski, V., Keller, C. U., Doelman, N., Fraanje, R., and Verhaegen, M., "Joint optimization of phase diversity and adaptive optics: demonstration of potential," *Applied Optics* **51**, 102 (Jan. 2012).

[10] Gonsalves, R. A., "Adaptive Optics by Sequential Diversity Imaging," in [*Beyond Conventional Optics*], E. Vernet, R. Ragazzoni, S. Esposito, & N. Hubin, ed., **58**, 121–+ (2002).

[11] Gonsalves, R. A., "Sequential Diversity Imaging: Phase Diversity with AO Changes as the Diversities," in [*Frontiers in Optics*], *OSA Technical Digest (CD)*, FWV1 (2010).

[12] Keller, C. U., Korkiakoski, V., Doelman, N., Fraanje, R., and Verhaegen, M., "Extremely fast focal-plane wavefront sensing for extreme adaptive optics," in [*Adaptive Optics Systems III*], *Proc. SPIE*, This conference (2012).

[13] Gonsalves, R. A., "Small-phase solution to the phase-retrieval problem," *Optics Letters* **26**, 684–685 (May 2001).

[14] "List of publications at okotech website." `http://www.okotech.com/publications`. Accessed: 10/06/2012.

[15] Roddier, F., "Theoretical aspects," in [*Adaptive Optics in Astronomy*], Roddier, F., ed., 25–56, Cambridge university press (1999).

[16] "yao." `http://frigaut.github.com/yao/index.html`. Accessed: 10/06/2012.

[17] Tyson, R. K., [*Principles of Adaptive Optics*], Academic Press, Inc., San Diego (1991).

[18] Paterson, C., Munro, I., and Dainty, J. C., "A low cost adaptive optics system using a membrane mirror," *Optics Express, vol. 6, Issue 9, p.175* **6**, 175 (Apr. 2000).

[19] Roberts, Jr., L. C., Perrin, M. D., Marchis, F., Sivaramakrishnan, A., Makidon, R. B., Christou, J. C., Macintosh, B. A., Poyneer, L. A., van Dam, M. A., and Troy, M., "Is that really your Strehl ratio?," in [*Advancements in Adaptive Optics. Edited by Domenico B. Calia, Brent L. Ellerbroek, and Roberto Ragazzoni. Proceedings of the SPIE, Volume 5490, pp. 504-515 (2004).*], Bonaccini Calia, D., Ellerbroek, B. L., and Ragazzoni, R., eds., **5490**, 504–515 (Oct. 2004).

[20] Korkiakoski, V., Vérinaud, C., and Le Louarn, M., "Improving the performance of a pyramid wavefront sensor with modal sensitivity compensation," *Applied Optics* **47**, 79–87 (2008).